Article

Understanding the Surface Oxidation of Ag Nanocrystals Under Different Environmental Conditions

Kyle D. Gilroy [1], Yutong Wang [2], and Younan Xia [1,2,3,4,*]

[1] The Wallace H. Coulter Department of Biomedical Engineering, Georgia Institute of Technology and Emory University, Atlanta, GA 30332, USA
[2] School of Chemistry and Biochemistry, Georgia Institute of Technology, Atlanta, GA 30332, USA
[3] Department of Materials Science and Engineering, Johns Hopkins University, Baltimore, MD 21218, USA
[4] Department of Biomedical Engineering, Johns Hopkins University, Baltimore, MD 21205, USA
* Correspondence: yxia70@jh.edu
Received: 3 March 2026; Revised: 17 March 2026; Accepted: 20 March 2026; Published: 23 March 2026

Abstract: In many cases, the presence of a shell of surface oxide detrimentally alters the properties of nanomaterials, rendering them ineffective for the targeted applications. This issue is yet to be addressed because the growth and removal of oxide(s) from the surface of nanomaterials is still poorly understood. In this article, we used vapor-phase-derived Ag nanocrystals with controlled sizes to elucidate the mechanisms of surface oxidation by exposing them to ambient atmosphere, aqueous environments, and ethylene glycol. Our experimental data suggested that the thickness of an oxide shell directly correlated with the extent of plasmon damping, and the optical properties of nanocrystals below 8 nm in size were more drastically affected by the presence of an oxide shell relative to larger counterparts. In addition, we found that aqueous environments with a relatively high pH gave rise to higher rates of oxidation. The time-dependent changes in optical properties were also validated using theoretical simulations based on the discrete dipole approximation. We concluded this article by discussing three different strategies for effectively removing the surface oxide, including decomposition through thermal annealing, wet-chemical reduction through the addition of a reducing agent, and decomposition and/or reduction by electron irradiation.

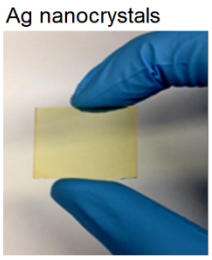

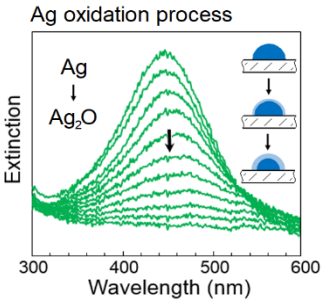

Keywords: oxidation; silver; nanocrystal; plasmon; discrete dipole approximation

1. Introduction

Oxidation is a redox reaction that involves the transfer of electrons from one chemical species to another. This fundamental process can be manipulated strategically to carry out vital electrochemical catalytic reactions, or to engineer the shape and structure of colloidal nanocrystals [1,2]. In other contexts, oxidation can also be considered a barrier, especially when structural materials such as steel are exposed to an oxidative environment, to suppress the continued formation of new materials (e.g., iron oxides in the case of steel) with unfavorable properties. Analogous issues arise in nanotechnology, where materials with nanoscale dimensions have an even higher susceptibility to oxidative environments such as air filled with oxygen or sulfur-containing compounds. Nanomaterials comprised of metals such as Fe, Ni, and Co can react with oxygen to generate metal oxides [3–5], while other metals such as Al, Cu, and Ag often form ultrathin, self-terminating oxide layers on the surface that can, in turn, protect the interior of the structure from further oxidation but at the same time hinder their performance in applications that demand pure metal interfaces [6–8]. Despite the rich history and great amount of work dedicated to the study of surface oxidation, very little is known about the kinetics, mechanisms, dependence on size down to the nanoscale regime, and strategies for preventing or removing the surface oxides.

In this study, we focused on the use of Ag nanocrystals supported on solid substrates as a model system to elucidate the nanoscale size effects and mechanisms that govern surface oxidation. It is worth pointing out that investigations into the oxidation of Ag date as far back as 1887, when Le Chatelier demonstrated the reversible

conversion between Ag and its oxidized form Ag_2O [9]. It was later discovered by Lewis in 1905 that the decomposition of Ag_2O was autocatalytic in nature [10]. In 2002, our group utilized the sensitive localized surface plasmon resonance (LSPR) of colloidal Ag nanocrystals (spectrally located in the visible region) as a direct means to monitor the surface oxidation process [8]. It is generally accepted that the oxidation involves the reaction between surface Ag atoms and gaseous O_2, which can be represented as $4\ Ag + O_2 \rightarrow 2\ Ag_2O$ [10–12]. However, limited work has been conducted to elucidate the mechanisms of oxide formation on Ag nanocrystals, and subsequently, how the oxides degrade the unique optical and chemical properties of nanomaterials. This gap in research likely stems from the fact that nanocrystals generated via wet-chemical methods as colloids are less than ideal for confidently quantifying the surface oxidation process, as they are commonly covered by a multitude of ions, organic capping agents and/or stabilizers, impurities from the solvent, and pre-adsorbed gas molecules. These adsorbates not only redefine the surface energy landscape of the nanocrystals and act as physical barriers to surface reactions, but also, more significantly, influence the optical and chemical properties [13].

To circumvent some of these drawbacks, a number of groups have shifted their focus to Ag nanocrystals supported on solid substrates. In these cases, the Ag nanocrystals can be fabricated *in vacuo* in the absence of the aforementioned chemical species that can obfuscate the oxidation mechanism. Furthermore, like a colloidal system, the ultrasensitive nature of LSPR (in terms of peak position and intensity) can still be used to track and quantify oxide formation [14]. In one study, Kalyanaraman and co-workers examined the oxidation of Ag nanocrystals (supported on SiO_2) formed through pulsed laser deposition (PLD). They found that indoor ambient air conditions led to a drastic change in both the composition and morphology, and subsequently, pronounced LSPR damping [15]. Sukhishvili and co-workers obtained a similar result for colloidal Ag nanocrystals deposited on a glass support and showed that the oxidation process led to deleterious effects in terms of surface-enhanced Raman spectroscopy (SERS), where the enhancement factor dropped by three orders of magnitude after the formation of a sub-monolayer of Ag_2O [11]. In this study, we investigate the oxidation process by subjecting size-controlled Ag nanocrystals on amorphous SiO_2 (a-SiO_2) supports to a variety of media to elucidate the nano-size effects and chemical mechanisms that govern Ag surface oxidation. We also demonstrate effective means for removing the oxide layer without compromising the optical properties of the nanocrystals.

2. Experimental Section

2.1. Chemicals and Materials

Silver (Ag, 99.99%), nitric acid (HNO_3), sodium hydroxide (NaOH), ethylene glycol (EG), amorphous SiO_2 (a-SiO_2) were all obtained from Sigma-Aldrich (St. Louis, MO, USA) and used as received. The SiO_2 TEM grids were purchased from TEMwindows.com (West Henrietta, NY, USA) with catalog number SO100-A40Q33. The deionized (DI) water used in the experiments was obtained from a Millipore ultrapure water system (Billerica, MA, USA) with a resistivity of 18.2 MΩ·cm at room temperature.

2.2. Synthesis of Ag Nanocrystals Supported on a-SiO_2

The Ag nanocrystals were prepared via thermal evaporation of Ag onto amorphous SiO_2 substrates following a previously reported procedure [16], in which the deposition conditions and thickness calibration were both described. Briefly, Ag was thermally evaporated from a tungsten boat to form Ag films with effective thicknesses of approximately 1.7, 0.5, 0.1, and 0.05 nm. The films were subsequently annealed at 600 °C for 2 min under vacuum and then cooled to room temperature over 2 h without breaking vacuum. During annealing, the continuous Ag films dewetted and evolved into discrete nanocrystals.

2.3. Characterizations

Transmission electron microscopy (TEM) was carried out with a Hitachi HT7700 microscope (Tokyo, Japan). For TEM analysis, the same deposition and annealing procedure described above were carried out on Si grids coated with a 40 nm a-SiO_2 layer. Optical extinction spectra were measured using a Cary 60 ultraviolet–visible (UV–vis) spectrometer. Samples were mounted inside the spectrometer so that the incident light beam was normal to the substrate surface. X-ray photoelectron spectroscopy (XPS) analyses were conducted using a Thermo K-Alpha system (Waltham, MA, USA). High-angle annular dark-field (HAADF) scanning transmission electron microscopy (STEM) images were acquired using a spherical aberration-corrected Hitachi HD2700 STEM microscope operated at 200 keV.

2.4. pH-Dependent Oxidation Studies

The pH of water derived from a Millipore system was controlled by adding HNO_3 or NaOH to decrease or increase the pH, respectively. After pH adjustment, the pH was measured using a standard electrode-based pH meter. To measure the pH-dependent rate of oxidation for the 4-nm Ag nanocrystals, the samples were placed in cuvettes filled with water with different pH values. It is found that samples derived from different batches would give inconsistent rates of oxidation because there always exists some degree of variation among different batches. To mitigate this issue, we deposited Ag on a relatively large piece of glass (~2.5 cm × 1 cm), annealed the sample, and then used a diamond scribe to cut the substrate into three similar-sized samples. Then, each sample was placed in a cuvette containing 1 mL of water with a pre-measured pH, and optical absorbance spectra were measured periodically at intervals of 3 min. It is assumed that each of the three pieces derived from the same batch had the same initial LSPR spectrum, and thus, this initial spectrum was used to represent the first data point for each of the three samples reported.

2.5. Formation of Thick Oxide Shells

To grow a thick oxide shell, Ag nanocrystals were first prepared and deposited on SiO_2 TEM grids, which were then mounted on a standard TEM holder. Then, the holder was inserted into a ZONE Desktop Sample Cleaner and Desiccator for SEM/TEM for roughly 5 min. The sample was then transferred to an aberration-corrected Hitachi HD-2700 TEM to monitor changes under the 200 keV electron beam.

3. Results and Discussion

3.1. Synthesis and Characterization of Ag Nanocrystals

We prepared the Ag nanocrystals by thermally evaporating Ag onto the surface of *a*-SiO_2 to form Ag films (Figure 1, top) following a reported procedure [16]. Specifically, we prepared Ag films of ca. 1.7, 0.5, 0.1, and 0.05 nm in effective thicknesses, annealed the samples at 600 °C for 2 min and then cooled to room temperature under vacuum. In each case, heating caused the film to evolve into discrete nanocrystals, changing the sample color from purple to vibrant yellow (Figure 1, bottom).

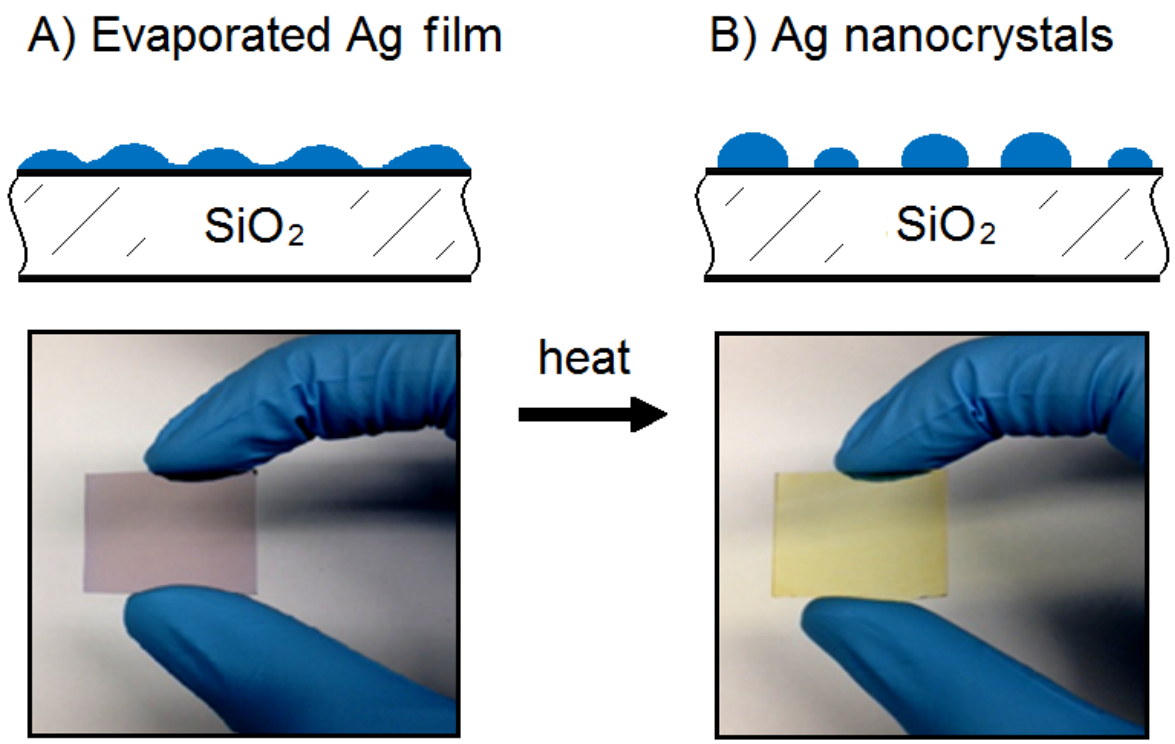

Figure 1. (**A**) Schematic illustration of a 1.7-nm Ag film deposited on an *a*-SiO_2 substrate by thermal evaporation with a corresponding photograph showing that the film appeared purple. (**B**) Upon annealing *in vacuo* at 600 °C and then cooling to room temperature, the Ag film dewetted and broke into discrete Ag nanocrystals, causing the sample to turn yellow.

Transmission electron microscopy (TEM) images revealed that the Ag nanocrystals derived from Ag films with effective thicknesses of ca. 1.7, 0.5, and 0.1 nm, respectively, had average diameters of 16, 8, and 4 nm (Figure 2A–C). Their size distributions were shown in Figure 2D. Note that the error in deposition thickness can be up to ±0.2 nm, and because the average diameter of the resultant particles trended logarithmically with deposition thickness [16], the average size can have an error of roughly ±2 nm. As another note, our group previously established that the internal defect structure (i.e., number and orientation of twin defects) trended with particle size post equilibration [16]. Under these conditions, Ag nanocrystals with icosahedral, decahedral, and single-crystal structures were found to be favored at sizes below 7 nm, between 7–11 nm, and greater than 11 nm, respectively. The optical properties of the Ag nanocrystals were further examined using UV–vis spectroscopy. Figure S1 shows the extinction spectra of Ag nanocrystals prior to oxidation. The LSPR peaks of all samples investigated in this work were positioned between 430–450 nm, and the LSPR peak intensity increased in proportion to the thickness of the Ag film.

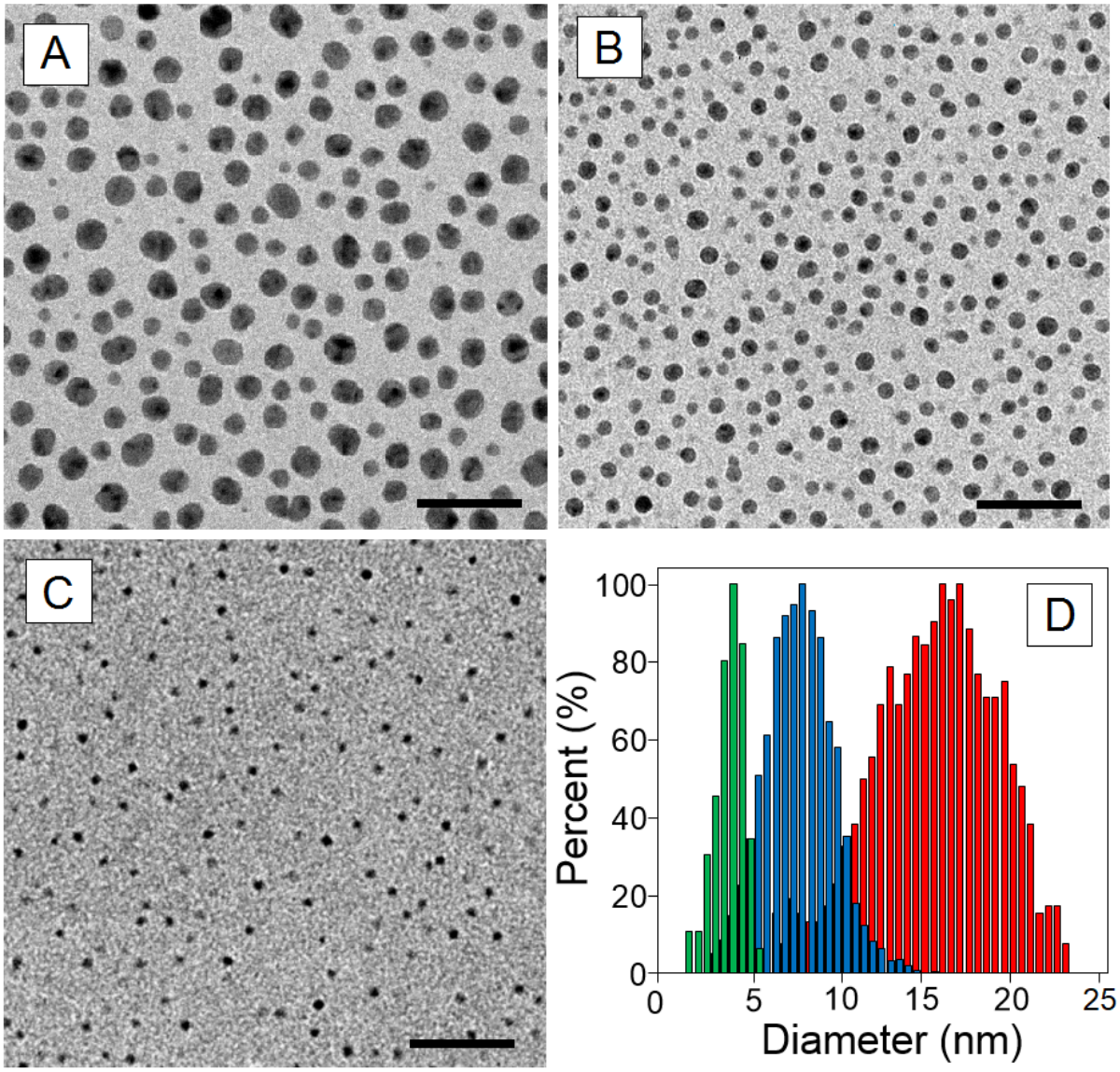

Figure 2. TEM images of Ag nanocrystals obtained by annealing Ag films of (**A**) 1.7; (**B**) 0.5; and (**C**) 0.1 nm, respectively, in thickness. (**D**) Histograms overlaid to show the size distributions of the Ag nanocrystals resulting from the films of 1.7, 0.5, and 0.1 nm in thickness, as represented by orange, blue, and green colors. All scale bars are 50 nm.

3.2. Oxidation Behaviors of Ag Nanocrystals under Diverse Conditions

We first examined the oxidation behavior of the Ag nanocrystals under ambient air conditions (23 °C, 50–60% humidity) by monitoring changes to their optical spectra in real time. Remarkably, for Ag nanocrystals of 4 nm or 8 nm in size, the changes could even be observed with the naked eye, with the sample changing from yellow to

transparent. For all three samples, the changes in spectral profile appeared to reach a steady state after 14 h, suggesting that (i) smaller particles generated thicker oxide layers and thereby underwent a greater degree of LSPR damping or (ii) the thickness of the oxide layer was size-independent, but the LSPR intensity of smaller particles was more heavily impacted by oxidation. For the LSPR peak position and intensity of the 16-nm Ag nanocrystals, only a slight red-shift and minor decrease in intensity were observed (Figure 3A). In the case of 8-nm Ag nanocrystals, optical changes consisted of a LSPR peak intensity drop of ca. 30% and a spectral red-shift of ca. 3 nm (Figure 3B). The greatest changes in optical signal corresponded to a ca. 85% drop in LSPR peak intensity along with a red-shift of ca. 40 nm, which were observed for Ag nanocrystals with an average diameter of 4 nm or below (Figure 3C).

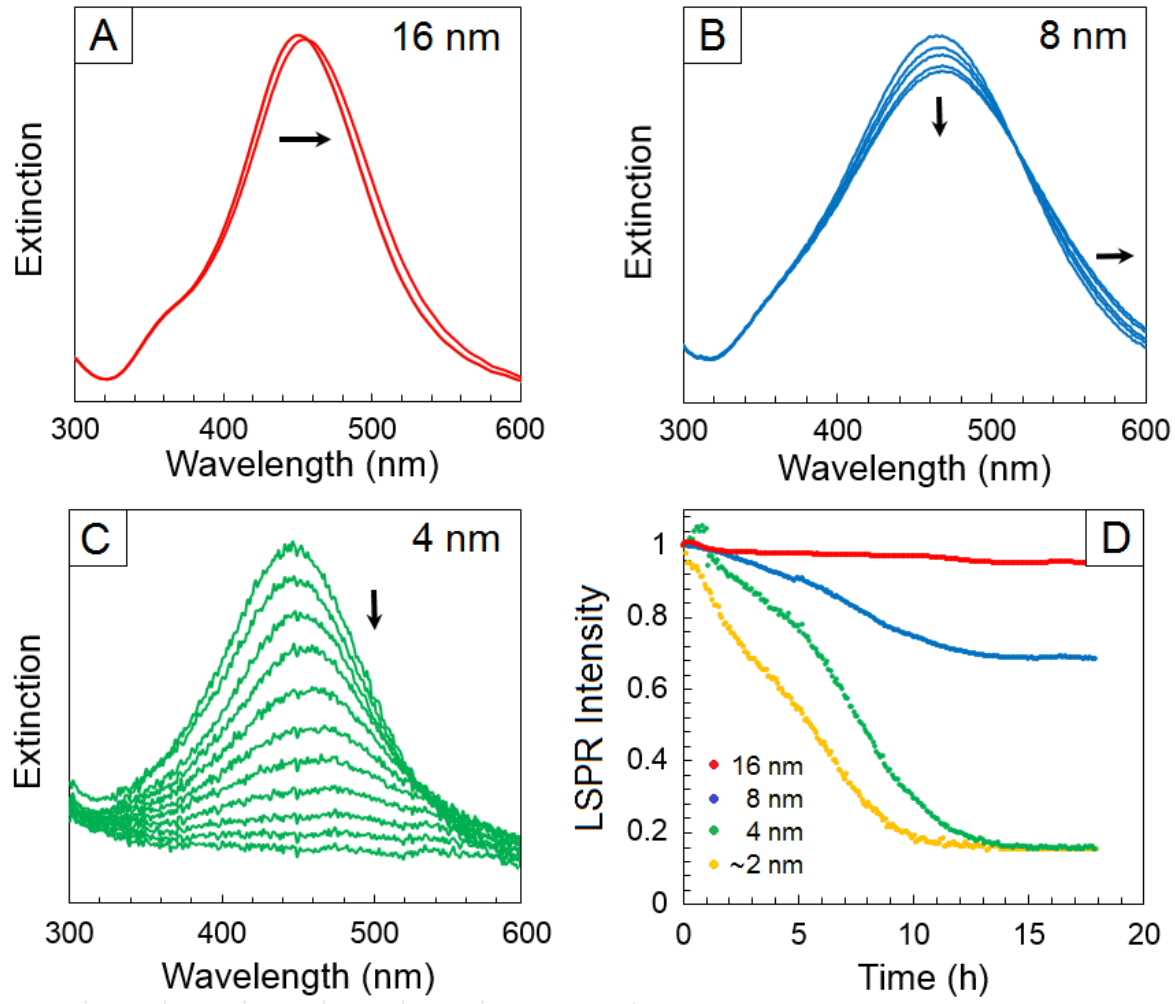

Figure 3. Spectral evolution of Ag nanocrystals with average diameters of (**A**) 16; (**B**) 8; and (**C**) 4 nm; respectively, upon exposure to the ambient air for up to 18 h. (**D**) Plots comparing the normalized extinction at the LSPR peak position as a function of the exposure time, revealing that atmospheric oxidation impacts the smaller particles more significantly.

To elucidate the role played by surface oxidation in determining the optical properties of Ag nanocrystals, we carried out simulations using the discrete dipole approximation (DDA) method [17]. To simulate the changes in LSPR upon oxidation, we designed a continuum model, as illustrated in Figure 4A, which consisted of an individual Ag_2O-coated Ag nanocrystal supported on a SiO_2 slab. At all sizes investigated, the calculated results indicated that increasing the thickness of the oxide shell led to peak damping and a slight red-shift, as shown for a 4-nm particle in Figure 4B. A red-shift in the LSPR band was generally attributable to an increase in the refractive index of the surrounding medium, which is consistent with the change from air to Ag_2O. In addition to this refractive index effect, the damping of the LSPR can be attributed to interband transitions in Ag_2O. Specifically, the band gap of Ag_2O falls within the visible region, enabling optical excitation of interband transitions that overlap with the plasmon resonance. These transitions introduce a significant imaginary component (ε_2) to the dielectric function, leading to additional absorption and energy dissipation, and thus damping the LSPR. The $\varepsilon_{Ag}(\lambda)$ and $\varepsilon_{Ag_2O}(\lambda)$ can be found in Figure S2. The degree of peak damping was found to trend exponentially with Ag_2O

thickness, while the LSPR peak intensities of smaller particles were more affected by oxide formation (Figure 4C). The inset in Figure 4C shows the changes in LSPR peak intensity as the thickness of the Ag_2O shell was increased up to 0.5 nm, with the experimentally measured LSPR damping, which was used to estimate an effective oxide thickness based on the DDA simulations, shown as squares. The peak intensity of the 4-nm Ag nanocrystals showed a drop of ca. 80% when the thickness of Ag_2O reached 0.25 nm (roughly one monolayer). However, for the same thickness of Ag_2O, the LSPR peak intensities of the 8- and 16-nm nanocrystals were only damped by ca. 70% and 30%, respectively; both values were significantly greater than what was observed experimentally (30% and 3%, respectively). These discrepancies suggested that only sub-monolayers of oxide were formed on the larger nanocrystals, as reported previously [11,18]. Since the surface free energy (and thus reactivity) of nanoparticles trended exponentially with size [19], it was feasible that the smaller nanocrystals were more prone to oxidation due to their higher reactivity.

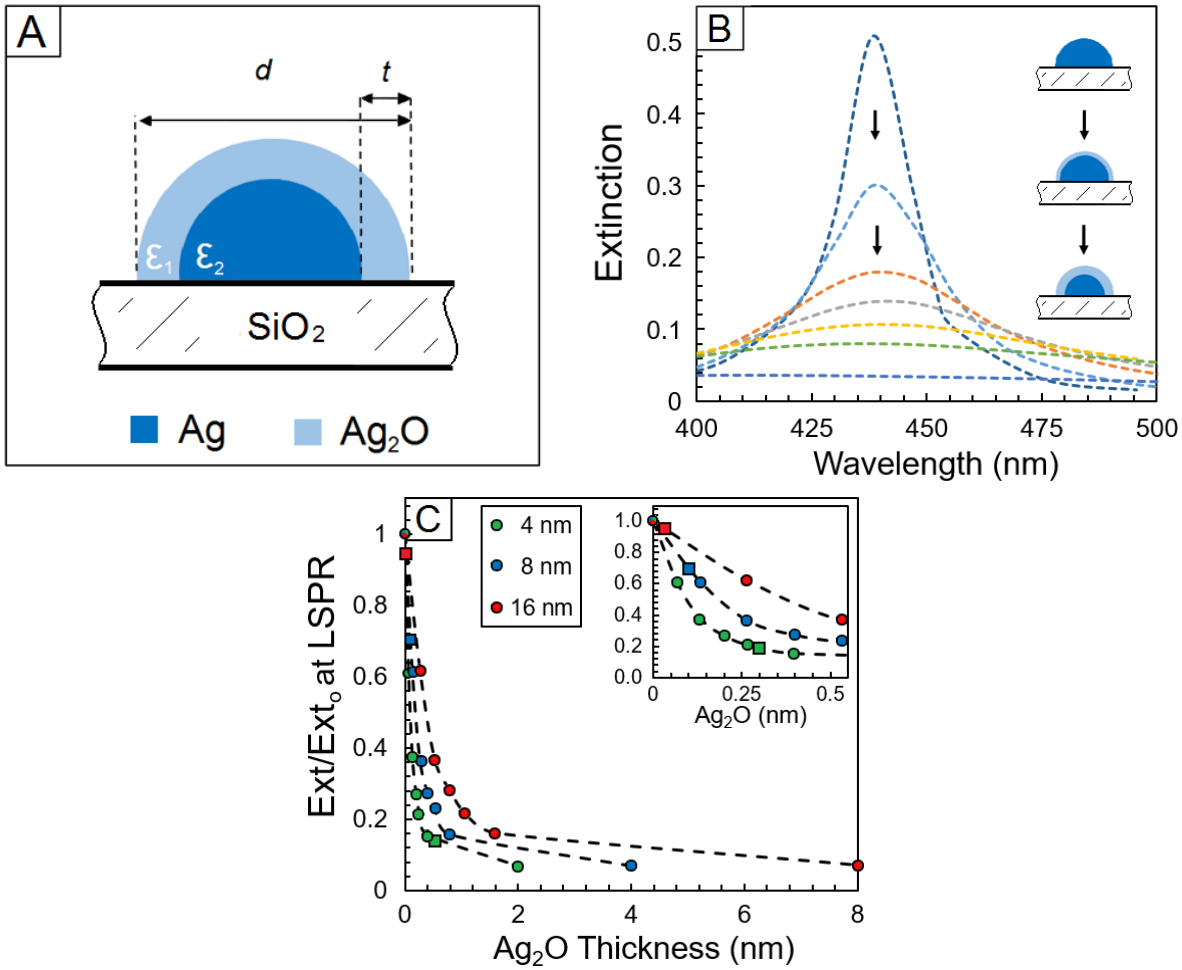

Figure 4. (**A**) Schematic illustration showing the continuum model on which all DDA simulations are based. The model consists of a Ag_2O-coated Ag hemisphere supported on a SiO_2 substrate. (**B**) Calculated extinction spectra of a 4-nm Ag hemisphere undergoing oxidation, where the increase in Ag_2O thickness leads to increased damping. (**C**) Theoretical trends showing the fractional change in LSPR peak intensity as a function of increasing Ag_2O thickness for Ag nanocrystals of 4, 8, and 16 nm in diameter. The experimentally measured LSPR damping, which was used to estimate an effective oxide thickness based on the DDA simulations, is represented by squares. The inset in (**C**) shows a zoomed-in view of the fractional change in peak intensity as the thickness of the Ag_2O shell is increased up to 0.5 nm.

LSPR damping upon the formation of an ultrathin oxide layer was similar to what has been observed when the surface of a metal nanocrystal with LSPR in the visible regime (e.g., Au, Ag, and Cu) is conformally coated with a platinum-group metal such as Pt, Pd, or Ir [20,21]. In essence, when the overlayer is sufficiently thick, it shields the inner core and severely damps the LSPR. In a similar fashion, formation of an ultrathin Ag_2O shell substantially damped the LSPR. It is important to note that the damping effect (due to oxide shell formation) is not unique to supported nanocrystals as our simulations also showed that 4-nm spherical Ag nanocrystals (i.e., reminiscent of Ag

colloids) also underwent substantial damping after the formation of a 0.25-nm complete Ag_2O shell (Figure S3). However, while the LSPR peak position and shift matched the experimental data, the calculated linewidth, and thus theoretical damping constant (Γ) was underestimated ($\Gamma_{exp} \sim 4\Gamma_{theory}$), as expected from the dielectric constants provided by Johnson and Christy [22]. In addition, further peak broadening is expected from enhanced electron-surface scattering for nanoparticles smaller than the electron mean-free path of bulk Ag ($l_{Ag}^{\infty} = 52$ nm) [23,24]. This effect was evident when the full width at half maximum (FWHM) of the LSPR peaks measured from the 4- and 16-nm Ag nanocrystals were compared, where the FWHM of the 4 nm nanocrystals was broader by 14 nm when compared to those of 16 nm in size (Figure S4).

To further evaluate the role of the surrounding medium, we next examined the oxidation behavior of the Ag nanocrystals in liquid environments. In practical applications, plasmonic nanocrystals are often used in solvents such as water or polyols [13,19]. To this end, it is critical to know how Ag nanocrystals respond to these environments as well. As another advantage of our system, the relatively strong interaction between the Ag nanocrystals and the substrate allowed us to immerse the sample in a solution prepared with a specific pH, ionic strength, and/or dielectric constant and then monitored the changes caused by the liquid environment [25]. Similar to the air-exposure experiments, we related the changes in optical properties to the thickness of the oxide grown at the surface of the Ag nanocrystals. All experiments involved submerging the samples in the liquid and placing them against the inside wall of a cuvette with the nanocrystal side of the sample facing the bulk of the solution. It should be noted that removing samples from water and allowing them to dry would cause some of the particles to lift off the surface. However, when the samples were submerged in water and then subjected to ultrasonication, the sample color remained bright yellow for hours (in the case of the 16-nm structures), suggesting that particles left the surface at a negligible rate during the oxidation experiments.

Realizing these aforementioned advantages, we investigated the oxidation of the 4-nm Ag nanocrystals in water and ethylene glycol (EG) and compared the results with what was obtained in the case of air (Figure 5A). To make a quantitative comparison among the three media in terms of oxidation rate, we derived rate constants based on the time-dependent change in LSPR peak intensity. Specifically, the time-dependent LSPR peak intensity changes were fitted using a first-order exponential decay function. The rate constant can then be extracted from the slope of the linear plot of $-\ln(I/I_0)$ versus time (Figure S5). The obtained rate constants ares primarily used for comparative analysis among different chemical conditions. The Ag nanocrystals exposed to EG showed the slowest oxidation rate, likely due to a number of effects but primarily from the formation of EG multilayers that could prevent the surface atoms from interacting with the oxygen dissolved in EG [26]. These adsorbed EG multilayers, with n and k of 1.4 and 4.3×10^{-8} at 450 nm [27], respectively, were not expected to induce a time-dependent change in optical properties. Furthermore, EG is a well-known reducing agent [28], which provides an additional measure against oxidation. In contrast, nanocrystals exposed to water showed the fastest rate of oxidation, where a steady state was reached within 1 h (pH = 6.8) with respect to the change in LSPR peak intensity.

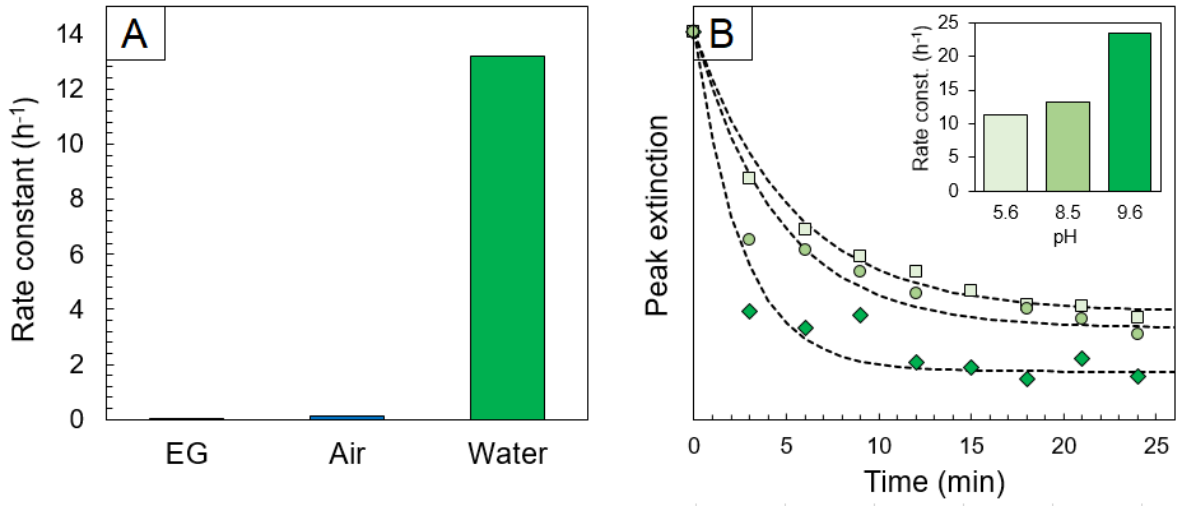

Figure 5. (**A**) Bar graph comparing the oxidation rate constant of 4-nm Ag nanocrystals in ethylene glycol (EG), air, and water (pH = 8.5). (**B**) Scatter plot showing the decrease in extinction intensity at the normalized LSPR peak for 4-nm Ag nanocrystals when subjected to aqueous environments at three different pH values (5.6, 8.5, and 9.6).

To further investigate the chemical mechanism, we measured the oxidation rate of the Ag nanocrystals derived from samples of the same batch in aqueous systems with different pH values. Our experimental results

clearly demonstrated that the oxidation rates correlated positively with increasing pH (Figure 5B). However, it should be noted that the rate of oxidation varied greatly between different batches, illustrating the high sensitivity of this process. Based on our results, we believed that the enhanced oxidation rate in water, relative to air and EG, was likely due to the high concentration of hydroxide ions (OH^-). This suggested that the oxidation process was accelerated in alkaline solutions due to the presence of OH^- species as depicted in Equations (1) and (2), in which the hydroxyl species are consumed in (1) and regenerated in (2). This led to the formation of AgOH that could easily decompose into Ag_2O and H_2O according to Equation (3). Taken together, these steps constitute the overall reaction scheme shown in Equation (4). For the same reason, oxidation under the ambient air conditions could also be driven by the presence of water molecules, which is supported by the work of Jiu and co-workers who showed that electrical contacts comprised of Ag-nanowire films oxidized more rapidly when exposed to atmospheric conditions at relatively high humidity [29].

$$4Ag + 4OH^- \rightarrow 4AgOH + 4e^- \quad (1)$$

$$2H_2O + O_2 + 4e^- \rightarrow 4OH^- \quad (2)$$

$$4AgOH \rightarrow 2Ag_2O + 2H_2O \quad (3)$$

$$4Ag + O_2 \rightarrow 2Ag_2O \quad (4)$$

To ensure that the observed oxidation behavior was intrinsic rather than arising from extrinsic factors, we also investigated the possible involvement of chemical contaminants. One common mode of Ag corrosion is sulfidation, where sulfur-containing compounds (e.g., H_2S) react with the Ag surface to form Ag_2S [30], a semiconducting material with drastically different optical properties. To rule out this possibility, X-ray photoelectron spectroscopy (XPS) was carried out, and no signals from sulfur-containing species were detected (Figure S6A). As another possibility, tungsten from the evaporation boat could also contaminate the Ag during the deposition process. However, the XPS measurements showed no evidence of tungsten-containing species (Figure S6B).

A contaminant that was naturally found within the sample was carbon, which could arise at any stage of sample preparation, including substrate cleaning and loading, during the deposition process, or even after the annealing through interactions with atmospheric hydrocarbons or gaseous CO_2. We carried out a series of XPS measurements before and after exposure to atmospheric conditions which revealed two distinct and universal spectral changes: (i) an increase in binding energy for the peak positions of both Ag $3d_{3/2}$ and Ag $3d_{5/2}$ and (ii) the disappearance of the energy loss feature. The XPS spectra in Figures 6A−C suggested the presence of carbonates (i.e., CO_3^{2-}) even prior to the long exposure to atmospheric conditions. Specifically, the initial Ag 3d peak position was located at 367.9 eV, which lies between the binding energies for Ag^0 (368.2 eV) and Ag_2CO_3 (367.7 eV). It is well-known that CO_2 strongly interacts with Ag_2O to produce Ag_2CO_3 through the following reaction: $Ag_2O + CO_2 \rightarrow Ag_2CO_3$ [30]. In fact, bulk Ag_2O has been actively explored as a thermally regenerable sorbent of CO_2 for purifying breathing air within space suits worn by astronauts during extravehicular activities [31]. We were able to rule out significant carbonation after the annealing step since Ag_2CO_3 readily decomposes at temperatures >200 °C. Interestingly, this carbonate layer has been attributed to the unique corrosion resistance properties of Ag [32]. Furthermore, previous XPS studies based on AgO and Ag_2O powders had shown that the CO_2 present in the air was responsible for generating Ag_2CO_3 on their surface [33,34]. In another study, by using XPS and SERS, it was found that exposing Ag nanocrystals to atmospheric conditions resulted in an exponential increase in the percentage of oxygen and carbon contamination after only 48 h, with the elemental percentages of Ag, O, and C reaching steady-state values of 66, 10, and 24%, respectively [35]. Despite the potential presence of Ag_2CO_3 at the surface, the optical characterization and simulation results suggested that it played a minor role in LSPR damping. Unfortunately, since the optical constants of Ag_2CO_3 are currently unavailable, we were unable to simulate its effect with our continuum model.

Our results also indicated that as the oxidation process proceeded, the Ag $3d_{5/2}$ peak increased in energy until it centered at 368 eV (the peak center for Ag_2O was located at 367.9 eV). As the Ag $3d_{5/2}$ peak shifted to a higher energy, the loss features in all the XPS spectra decreased in intensity (Figure 6D−F). This trend was consistent with optical measurements that showed substantial LSPR damping following surface oxidation. In essence, the loss features could serve as a qualitative indicator of plasmon-related energy loss, since this signal was comprised of electrons that were extrinsic in nature, emanating from the released Ag $3d_{3/2}$ electrons that lost energy by stimulating the LSPR of the Ag nanocrystals before making it to the detector [36]. By subtracting the energy of the loss peak from that of the Ag $3d_{3/2}$ peak, it was found that these electrons lost 2.7 eV, a value almost equal to the energy of the LSPR located at ca. 450 nm (E_p = 2.76 eV) (see Figure S7 for clarification). It should be noted

that the changes in loss features may also be influenced by the sensitivity of XPS and the formation of Ag_2O layer, which can reduce the contribution from the underlying metallic Ag. Therefore, the decrease in the loss features is interpreted as being consistent with, rather than a direct measure of, the plasmon damping observed in the optical spectra. This conclusion was supported by Figures 3 and 4, which showed that Ag_2O-shell formation damped the LSPR peak, especially for the particles smaller than 4 nm.

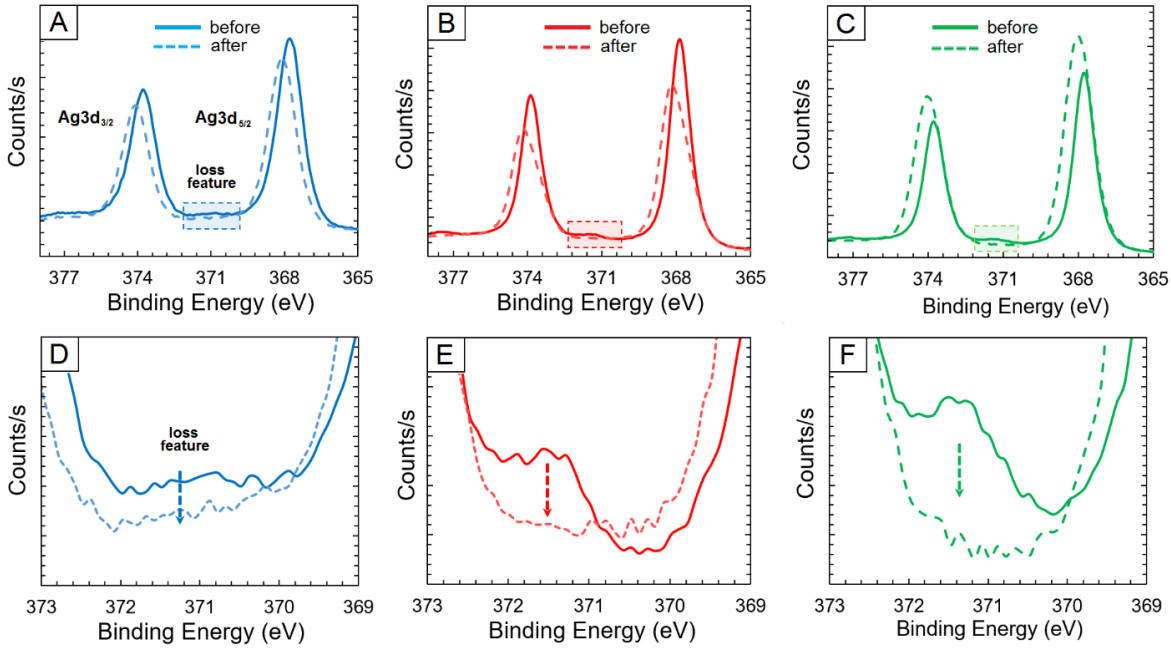

Figure 6. XPS spectra measured over the Ag $3d_{3/2}$ and Ag $3d_{5/2}$ spectral regions for (**A**) 4-nm nanocrystals; (**B**) 16-nm nanocrystals; and (**C**) a 1.5-nm Ag thin film before and after oxidation under ambient conditions; (**D**–**F**) XPS spectra showing the loss features associated with the corresponding spectra in (**A**–**C**) (highlighted by a rectangular box) before and after the oxidation.

Taken together, our data suggest a multi-step oxidation process that begins with the formation of surface carbonates, followed by subsurface oxidation events leading to the formation of an ultrathin Ag_2O shell, a process that correlated positively with pH. This scenario fits well within the framework of the known literature, where the synthesis of Ag_2O nanocrystals was often found to be most effective when performed at elevated pH [37–39]. This was roughly consistent with what was expected from the Pourbaix diagram, which provides potential–pH boundaries for the most thermodynamically favorable oxidation processes of Ag metal (e.g., Ag, Ag^+, and Ag_2O), but with differences expected for the surface of Ag nanocrystals as compared to bulk Ag [40]. In essence, under wet conditions, the surface-based Ag_2O phase was likely to be the most stable in systems that had high pH values. As a final note, those who have investigated oxidation of Ag bulk electrodes in alkaline media have found the surface oxidation process to be highly complex, involving a series of steps, including the adsorption of OH^- ions, solid-state diffusion, Ag or Ag oxide dissolution, and a change in surface roughness [41].

3.3. Removal of Surface Oxides from Ag Nanocrystals

The surface oxidation of Ag nanocrystals is detrimental to many applications that rely on either the strong LSPR or the unique electronic structure of surface Ag atoms. Therefore, it is essential to develop methods capable of removing the surface oxide layer without compromising the underlying Ag atoms. Here we focused on three methods, including thermal decomposition, chemical reduction, and electron beam irradiation.

The most straightforward way to remove surface oxide and carbonaceous species is through thermal annealing. Heating to temperatures within the interval of 167−194 °C has been shown previously to decompose Ag_2CO_3 [42]. In terms of silver oxide removal, previous studies have shown that heating Ag_2O powders to temperatures upwards of 490 °C effectively removes both oxides and carbonaceous contaminants through decomposition, leaving behind pure Ag [33]. This same strategy was adopted for nanocrystals, as evidenced by the complete recovery of the LSPR after annealing for 2 min at 600 °C, as shown in Figure 7A. The slight decrease in intensity post annealing was likely due to the loss of Ag atoms or some small amount of residual oxide.

Another effective strategy involved the addition of a reducing agent. Since Ag_2O has a standard reduction potential (E^o) of 0.34 V vs. standard hydrogen electrode (SHE), the formation of Ag^0 via reduction of Ag^+ is thermodynamically favored when a reducing agent with $E^o_{Red} < E^o_{Ag_2O}$ is used [43]. To illustrate this concept, we simply subjected a partially oxidized sample to a 1 mL solution of ethanol (E^o = 0.20 V vs. SHE), which immediately led to recovery of the LSPR signal, as shown in Figure 7B.

As the least convenient oxide removal strategy, we found that electron irradiation was also viable. To illustrate this concept, we first synthesized Ag@Ag_2O core-shell nanocrystals with thick shells by exposing the 16-nm Ag nanocrystals to O_3 for ~5 min (by placing the sample in an ozone cleaner). This led to the formation of a thick Ag_2O oxide shell that encapsulated a Ag core (see Figure 7C). Notably, the oxide shells derived from atmospheric oxidation were undetectable by scanning transmission electron microscopy (STEM), likely due to the fact that ultrathin oxide shells rapidly decomposed upon exposure to the electron beam. When irradiating an individual Ag@Ag_2O particle with 200 keV electrons for 30 min, the core-shell particle transformed into a pure Ag nanocrystal, as demonstrated by the high-angle annular dark-field (HAADF) images in Figure 7C. In terms of mechanism, removal of the oxide shell could be driven by thermal decomposition or by reduction of Ag^+ by the high-energy electrons. Taken together, either chemically reducing Ag^+ or decomposing the Ag^+ compounds could be used to generate Ag nanocrystals with clean, oxide-free surfaces.

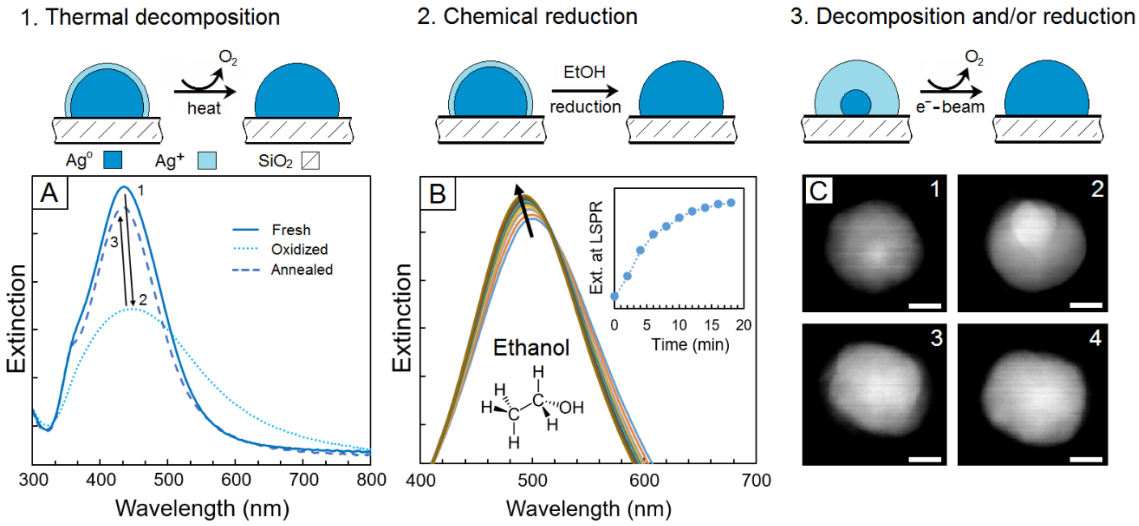

Figure 7. Summary of three effective strategies for removing the oxide layer from the surface of Ag nanocrystals. (**A**) Thermal decomposition, in which the sample was annealed at 600 °C post-oxidation from air, resulted in recovery of the LSPR to its initial spectral profile. (**B**) Chemical reduction, in which the structures were exposed to pure ethanol at room temperature after partial oxidation, also resulted in recovery of the LSPR signal. (**C**) Decomposition and/or reduction, in which an individual Ag@Ag_2O core-shell structure was monitored using HAADF-STEM, showing the growth of the Ag core (brighter region) at the expense of the Ag_2O shell (dimmer region) under 200 keV electron irradiation. The scale bars in (**C**) are all 5 nm.

4. Conclusions

In summary, surface-based Ag nanocrystals were synthesized with sizes ranging from 4–16 nm and then exposed to a variety of conditions while their LSPR spectra were monitored. It was found that the smaller particles underwent a much greater degree of plasmonic damping over the same period of time. All changes in the LSPR peak position and intensity were in agreement with theoretical modeling based on the DDA method, which showed that the degree of damping was commensurate with the thickening of a surface layer of Ag_2O. We also found that the rate of oxidation was greatest in aqueous environments relative to air and ethylene glycol, which we attributed to the presence of hydroxide ions that promoted the oxidation process. We measured the oxidation rate of the 4-nm Ag nanocrystals in a series of aqueous solutions with increasing pH, which revealed that the increased concentration of hydroxide ions accelerated the oxidation process. Analysis of the surface chemistry by XPS suggested that the oxidation process occurred in a series of steps, including a rapid two-step oxidation/carbonation process that was followed by subsurface oxidation events leading to Ag_2O formation. In addition to XPS measurements, these conclusions were supported by the time-dependent LSPR damping as well as the decrease in intensity of the XPS loss peak. Ultimately, after oxidation, the steady-state configuration was an Ag nanocrystal encapsulated by a self-terminating ultrathin Ag_2O shell, together with Ag_2CO_3 on the outermost surface.

In addition to understanding the size effect on the oxidation of Ag nanocrystals, we also demonstrated a variety of methods for removing the oxide and carbonate layers, including thermal decomposition through annealing, chemical reduction through the addition of a reducing agent, and electron irradiation during STEM. In the first two cases, recovery of the LSPR to its initial state provided direct evidence of oxide removal. In the latter case, we directly observed a decrease in the Ag_2O shell thickness as the Ag core increased in size. While all methods were effective in removing the oxide layer, these results also raise a number of additional perspectives. For example, those working with colloidal nanomaterials in aqueous systems likely have ultrathin oxide layers encapsulating their particles. However, if these particles are maintained in the presence of a reducing agent or at relatively low pH values, formation of the oxide layer can be minimized. These results are also important to those employing Ag nanocrystals as heterogeneous catalysts, since their performance is directly linked to the chemical state of the outermost atoms. To develop a more meaningful correlation between the substantial literature on colloidal Ag nanocrystals and the results discussed herein, future investigations must include systematic studies involving chemical adsorbates typical of colloidal systems (e.g., stabilizers, ligands, and reducing agents).

Supplementary Materials: The following supporting information can be downloaded at: https://media.sciltp.com/articles/others/2603231122380529/MI-26030014-SM.pdf. Figure S1: Extinction spectra of Ag nanocrystals derived from Ag films with effective thicknesses of <1, 1, 5, and 15 Å. The inset shows the LSPR peak intensity as a function of Ag film thickness, revealing a linear relationship; Figure S2: The dielectric constants of (A) Ag and (B) Ag_2O used for the DDA simulation. The dielectric functions (ε_1 and ε_2) of Ag and Ag_2O were obtained from literature reports [1,2] and used to generate the plots; Figure S3: DDA simulation of the extinction spectra of a 4-nm Ag nanocrystal before oxidation (blue) and after formation of a 0.25-nm shell of Ag_2O (green). These results suggest that the high sensitivity of LSPR to surface oxidation is not unique to the hemispherical nanoparticles supported on a substrate. The simulation was carried out with a surrounding dielectric constant equal to that of water ($\varepsilon_m = 1.78$); Figure S4: Normalized extinction spectra of the 4- and 16-nm Ag nanocrystals, showing that the FWHM of the LSPR was broader for the 4-nm sample; Figure S5: Plot of the LSPR peak intensity as a function of time (blue line), which is fitted with an exponential decay function with a rate constant of *k*. The rate constant can also be obtained from the slope of the linear plot of –ln(y) versus time (orange line); Figure S6: XPS spectra of the (A) sulfur 2p region and (B) tungsten 4f region measured from a typical Ag sample (derived from the 0.4-nm film), confirming the absence of sulfur- and tungsten-based contaminants; Figure S7: XPS spectrum of the Ag $3d_{3/2}$ region and associated loss feature, showing an energy separation of 2.7 eV. References [44,45] are cited in supplementary materials.

Author Contributions: K.D.G.: conducted experiments on materials preparation, oxidation monitoring, and analyzed the data; K.D.G. and Y.W.: prepared the manuscript. Y.X.: conceptualization, supervision, writing—reviewing and editing. All authors have read and agreed to the published version of the manuscript

Funding: This research was funded by a grant from NSF (CHE 2504965) and start-up funds from the Georgia Institute of Technology.

Data Availability Statement: The data that support the findings of this study are available from the corresponding author Y.X. upon reasonable request.

Acknowledgments: The authors gratefully acknowledge Zachary D. Hood, Madeline Vara, Thenner Silva Rodrigues, Anderson Gabriel Marques da Silva, and Jane Howe for their contributions to materials characterization.

Conflicts of Interest: The authors declare no conflicts of interest. Given the role as Editor-in-Chief, Y.X. was not involved in the peer review of this paper and had no access to information regarding its peer-review process. Full responsibility for the editorial process of this paper was delegated to another editor of the journal.

Use of AI and AI-Assisted Technologies: No AI tools were utilized for this paper.

References

1. Long, R.; Zhou, S.; Wiley, B.J.; Xiong, Y. Oxidative Etching for Controlled Synthesis of Metal Nanocrystals: Atomic Addition and Subtraction. *Chem. Soc. Rev.* **2014**, *43*, 6288–6310.
2. Sun, X.; Kim, J.; Gilroy, K.D.; Liu, J.; König, T.A.F.; Qin, D. Gold-Based Cubic Nanoboxes with Well- Defined Openings at the Corners and Ultrathin Walls Less Than Two Nanometers Thick. *ACS Nano* **2016**, *10*, 8019–8025.
3. Ling, D.; Lee, N.; Hyeon, T. Chemical synthesis and assembly of uniformly sized iron oxide nanoparticles for medical applications. *Acc. Chem. Res.* **2015**, *48*, 1276–1285.
4. Prieto, P.; Nistor, V.; Nouneh, K.; Oyama, M.; Abd-Lefdil, M.; Díaz, R. XPS Study of Silver, Nickel and Bimetallic Silver–Nickel Nanoparticles Prepared by Seed-Mediated Growth. *Appl. Surf. Sci.* **2012**, *258*, 8807–8813.
5. Ha, D.H.; Moreau, L.M.; Honrao, S.; Hennig, R.G.; Robinson, R.D. The Oxidation of Cobalt Nanoparticles into Kirkendall-Hollowed CoO and Co_3O_4: The Diffusion Mechanisms and Atomic Structural Transformations. *J. Phys. Chem. C* **2013**, *117*,14303–14312.
6. Knight, M.W.; King, N.S.; Liu, L.; Everitt, H.O.; Nordlander, P.; Halas, N.J. Aluminum for Plasmonics. *ACS Nano* **2014**, *8*, 834–840.

7. Jeong, S.; Woo, K.; Kim, D.; Lim, S.; Kim, J.S.; Shin, H.; Xia, Y.; Moon, J. Controlling the Thickness of the Surface Oxide Layer on Cu Nanoparticles for the Fabrication of Conductive Structures by Ink-Jet Printing. *Adv. Funct. Mater.* **2008**, *18*, 679–686.
8. Yin, Y.; Li, Z.Y.; Zhong, Z.; Gates, B.; Xia, Y.; Venkateswaran, S. Synthesis and Characterization of Stable Aqueous Dispersions of Silver Nanoparticles Through the Tollens Process. *J. Mater. Chem.* **2002**, *12*, 522–527.
9. Le Chatelier, H.; Über die Oxydation des Silbers. *Z. Phys. Chemie* **1887**, *1*, 516–518.
10. Lewis, G.N.; Zersetzung von Silberoxyd durch Autokatalyse. *Z. Phys. Chemie* **1905**, *52*, 310–326.
11. Han, Y.; Lupitskyy, R.; Chou, T.-M.; Stafford, C.M.; Du, H.; Sukhishvili, S. Effect of Oxidation on Surface-enhanced Raman Scattering Activity of Silver Nanoparticles: A Quantitative Correlation. *Anal. Chem.* **2011**, *83*, 5873–5880.
12. L'vov, BV. Kinetics and Mechanism of Thermal Decomposition of Silver Oxide. *Thermochimica Acta* **1999**, *333*, 13–19.
13. Xia, Y.; Xiong, Y.; Lim, B.; Skrabalak, S.E. Shape-controlled Synthesis of Metal Nanocrystals: Simple Chemistry Meets Complex Physics? *Angew. Chem. Intl. Ed.* **2009**, *48*, 60–103.
14. Mayer, K.M.; Hafner, J.H. Localized Surface Plasmon Resonance Sensors. *Chem. Rev.* **2011**, *111*, 3828–3857.
15. Sachan, R.; Ramos, V.; Malasi, A.; Yadavali, S.; Bartley, B.; Garcia, H.; Duscher, G.; Kalyanaraman, R. Oxidation-resistant Silver Nanostructures for Ultrastable Plasmonic Applications. *Adv. Mater.* **2013**, *25*, 2045–2050.
16. Gilroy, K.D.; Puibasset, J.; Vara, M.; Xia, Y. On the Thermodynamics and Experimental Control of Twinning in Metal Nanocrystals. *Angew. Chem. Int. Ed.* **2017**, *129*, 8773–8777.
17. Draine, B.T.; Flatau, P.J. Discrete-dipole Approximation for Scattering Calculations. *J. Opt. Soc. Am.* **1994**, *11*, 1491–1499.
18. Graedel, T. Corrosion Mechanisms for Silver Exposed to the Atmosphere. *J. Electrochem. Soc.* **1992**, *139*, 1963–1970.
19. Medasani, B.; Park, Y.H.; Vasiliev, I. Theoretical Study of the Surface Energy, Stress, and Lattice Contraction of Silver Nanoparticles. *Phys. Rev. B* **2007**, *75*, 235436.
20. Gilroy, K.D.; Ruditskiy, A.; Peng, H.C.; Qin, D.; Xia, Y. Bimetallic Nanocrystals: Syntheses, Properties, and Applications. *Chem. Rev.* **2016**, *116*, 10414–10472.
21. Cortie, M.B.; McDonagh, A.M. Synthesis and Optical Properties of Hybrid and Alloy Plasmonic Nanoparticles. *Chem. Rev.* **2011**, *111*, 3713–3735.
22. Blaber, M.G.; Henry, A.I.; Bingham, J.M.; Schatz, G.C.; Van Duyne, R.P. LSPR Imaging of Silver Triangular Nanoprisms: Correlating Scattering with Structure Using Electrodynamics for Plasmon Lifetime Analysis. *J. Phys. Chem. C* **2012**, *116*, 393–403.
23. Kreibig, U.; Vollmer, M. *Optical Properties of Metal Clusters*; Springer: Berlin/Heidelberg, Germany, **1995**, p. 79.
24. Hartland, G.V. Optical Studies of Dynamics in Noble Metal Nanostructures. *Chem. Rev.* **2014**, *111*, 3858–3887.
25. Gilroy, K.D.; Xia, Y. Dimerization of Colloidal Particles Through Controlled Aggregation for Enhanced Properties and Applications, *Chem. Asian J.* **2016**, *11*, 2341–2351.
26. Vodyankina, O.V.; Kurina, L.N.; Izatulina, G.A. Surface Interaction of Ethylene Glycol with Silver. *React. Kinet. Catal. Lett.* **1998**, *64*, 103–108.
27. Sani, E.; Dell'Oro, A. Optical Constants of Ethylene Glycol Over an Extremely Wide Spectral Range. *Opt. Mater.* **2015**, *37*, 36–41.
28. Li, C.; Shuford, K.L.; Park, Q.H.; Cai, W.; Li, Y.; Lee, E.J.; Cho, S.O.; High-Yield Synthesis of Single-Crystalline Gold Nano-octahedra. *Angew. Chem.* **2007**, *119*, 3328–3332.
29. Jiu, J.; Wang, J.; Sugahara, T.; Nagao, S.; Nogi, M.; Koga, H.; Suganuma, K.; Hara, M.; Nakazawa, E.; Uchida, H. The Effect of Light and Humidity on the Stability of Silver Nanowire Transparent Electrodes. *RSC Adv.* **2015**, *5*, 27657−27664.
30. Levard, C.; Hotze, E.M.; Colman, B.P.; Dale, A.L.; Truong, L.; Yang, X.Y.; Bone, A.J.; Brown, G.E.; Tanguay, R.L.; Di Giulio, R.T.; et al. Sulfidation of Silver Nanoparticles: Natural Antidote to their Toxicity. *Environ. Sci. Technol.* **2013**, *47*, 13440−13448.
31. Atwater, J.E.; Holtsnider, J.T.; Wheeler, R.R., Jr. *Microwave Regenerable Air Purification Device*; National Technical Information Service: Springfield, VA, USA, 1996.
32. Hoflund, G.B.; Hazos, Z.F. Surface Characterization Study of Ag, AgO, and Ag_2O Using X-ray Photoelectron Spectroscopy and Electron Energy-loss Spectroscopy. *Phys. Rev. B* **2000**, *62*, 11126.
33. Weaver, J.F.; Hoflund, G.B. Surface Characterization Study of the Thermal Decomposition of Ag_2O. *Chem. Mater.* **1994**, *6*, 1693–1699.
34. Weaver, J.F.; Hoflund, G.B. Surface Characterization Study of the Thermal Decomposition of AgO. *J. Phys. Chem.* **1994**, *98*, 8519–8524.
35. Matikainen, A.; Nuutinen, T.; Itkonen, T.; Heinilehto, S.; Puustinen, J.; Hiltunen, J.; Lappalainen, J.; Karioja, P.; Vahimaa, P. Atmospheric Oxidation and Carbon Contamination of Silver and its Effect on Surface-enhanced Raman Spectroscopy (SERS). *Sci. Rep.* **2016**, *6*, 37192.

36. Bates, C.W.; Wertheim, G.K.; Buchanan, D.N.E. Nature of the 3.8 eV Plasmon in X-ray Photoemission from Silver. *Phys. Lett. A.* **1979**, *72*, 178–180.
37. Kim, M.J.; Cho, Y.S.; Park, S.H.; Huh, Y.D. Facile Synthesis and Fine Morphological Tuning of Ag_2O. *Cryst. Growth Des.* **2012**, *12*, 4180−4185.
38. Wang, X.; Wu, H.F.; Kuang, Q.; Huang, R.B.; Xie, Z.X.; Zheng, L.S. Shape-dependent Antibacterial Activities of Ag_2O Polyhedral Particles. *Langmuir* **2010**, *26*, 2774–2778.
39. Kim, M.J.; Kim, S.; Park, H.; Huh, Y.D. Morphological Evolution of Ag_2O Microstructures from Cubes to Octapods and their Antibacterial Activities. *Bull. Korean Chem. Soc.* **2011**, *32*, 3793–3795.
40. Holewinski, A.; Idrobo, J.C.; Linic, S. High-performance Ag–Co Alloy Catalysts for Electrochemical Oxygen Reduction. *Nature Chem.* **2014**, *6*, 828–834.
41. Mayer, S.T.; Muller, R.H. Nucleation of Silver (I) Oxide Investigated by Spectroscopic Ellipsometry. *J Electrochem. Soc.* **2005**, *152*, A179–A185.
42. Kadlec, O.; Dubinin, M.M. Investigation of Kinetics of Thermal Decomposition of Solids. Communication 2. Thermal Decomposition of Silver Carbonate. *Izv. AN. SSSR. Otd. Khim. Nauk.* **1961**, *3*, 390–396. (In Russian)
43. Bratsch, S.G.J. Standard Electrode Potentials and Temperature Coefficients in Water at 298.15 K. *Phys. Chem. Ref. Data* **1989**, *18*, 1–21.
44. Johnson, P.B.; Christy, R.W. Optical Constants of the Noble Metals. *Phys. Rev. B* **1972**, *6*, 4370–4379.
45. Gao, X.Y.; Wang, S.Y.; Li, J.; Zheng, Y.X.; Zhang, R.J.; Zhou, P.; Yang, Y.M.; Chen, L.Y. Study of Structure and Optical Properties of Silver Oxide Films by Ellipsometry, XRD and XPS Methods. *Thin Solid Films* **2004**, *455–456*, 438–442.